Fisher, A., Davis, E.E., and Escutia, C. (Eds.), 2000
*Proceedings of the Ocean Drilling Program, Scientific Results,* Vol. 168

# 3. CORE-LOG-SEISMIC INTEGRATION IN HEMIPELAGIC MARINE SEDIMENTS ON THE EASTERN FLANK OF THE JUAN DE FUCA RIDGE[1]

Y.F. Sun[2]

**ABSTRACT**

The elastic properties of a sedimentary layer overlying young oceanic crust are investigated using field measurements and theoretical modeling. Based on a previously established dynamical theory of porous media, we further develop a theoretical model of velocity-porosity relationships for marine sediments. This physical model is in principle valid for the full porosity range from 0% to 100% and has many advantages over other empirical or semiempirical models. A new, critical parameter is defined as the flexibility factor of a formation that characterizes the softness or "uncompactedness" of the formation. It is found to be closely related to the sediment thickness and age. Nine sites were studied along a transect extending more than 100 km eastward from the Juan de Fuca Ridge, drilled during Ocean Drilling Program Leg 168 in 1996. The values of this flexibility factor decrease from 15 to 7 as the age of the sediment/basement contact along this transect increases from 0.9 to 3.6 Ma.

Integrating independent core, log, and seismic measurements using the proposed velocity-porosity model, we are able to provide high-resolution velocity-depth and porosity-depth profiles at all nine sites, although in situ logs were recorded at only one location. These derived velocity profiles help to obtain a more accurate time-depth model and to constrain a two-dimensional depth model of the sediment/basement contact, which is important for hydrological modeling and borehole observatory installations. The derived porosity-depth profiles are also useful to construct two-dimensional and three-dimensional models of other physical properties such as permeability and thermal conductivity.

Synthetic seismograms generated with these data agree well with field seismic data at all the sites along this transect, including good matches in traveltime, amplitude, and waveform. Using the log data at one site to correct for elastic rebound effects, continuous and discrete laboratory measurements of bulk density provide more reliable information than laboratory velocity measurements to construct synthetics for shallow depths. This process is repeated for the continuous density records (GRAPE density) at the other eight sites. Using generalized nonlinear inversion of parameterized seismic waveforms and the physical velocity-porosity model, iterative comparisons of field and synthetic seismic data are performed to estimate the flexibility factor in the model and to obtain optimal velocity-depth profiles. The proposed physical model is found to be suitable for the marine sediments at these sites and may be valid in other similar sedimentary environments.

## INTRODUCTION

The knowledge of the three-dimensional (3-D) structural and petrophysical properties of marine sediments is fundamental for many investigations towards the understanding of physical and chemical interactions of the ocean and the oceanic crust. The existence of a sediment cover overlying the ocean crust strongly affects fluid circulation between the ocean and the basement formation. Delineation of the thickness and structural stratigraphy of the sedimentary layer is important for determination of the hydrothermal flow patterns in the upper crust. The efficiency of this natural cover as a hydrothermal seal to the underlying active hydrothermal regime is largely defined by the sediment properties. The success of hydrothermal studies thus depends upon accurate knowledge of the in situ permeability, thermal conductivity, pressure, and temperature gradients in both the active hydrothermal regimes in the upper oceanic basement and the overlying sediment cover.

The physical properties of sediments and natural rocks are strongly influenced by environmental conditions, especially in situ pressure and temperature. Important among these physical properties are the porosity, bulk density, velocity, permeability, and thermal conductivity. Measurements of these properties made on the core samples in the laboratory need to be corrected for deviations from the natural in situ conditions. Another challenging problem is to estimate in situ properties in shallow high-porosity sediments that cannot be reliably measured in the laboratory. Accurate velocity-depth profiles under this condition allow for time-to-depth conversion of seismic reflection data. Velocity-depth profiles are used to assess the sediment/basement interfaces and other geological stratigraphic events (Davis et al., 1997) and to calculate porosity depth, thermal conductivity–depth profiles, and the subsurface thermal structure (Davis and Villinger, 1992). These relationships are usually approximated, however, by empirical or semiempirical models, and often by polynomial fits of field measurements (e.g., Hamilton, 1971; Jarrard et al.,1989; Davis and Villinger, 1992; Hyndman et al., 1993). In this report, we examine these relationships in a more general theoretical framework of poroelasticity. Such relationships may be applicable to different sedimentary environments of a wider porosity range.

We obtain high-resolution density-depth, porosity-depth, and velocity-depth profiles by combining the proposed theoretical model with a synthesis of three independent field measurements: core, log, and seismic data. The advantages of core-log-seismic integration is that these three independent measurements exploit different ranges of measurement frequency and investigate different scales of sediment property information. When integrated together, more reliable and complete knowledge of sediment properties is possible than when they are used separately.

Core measurements made under controlled conditions reveal the physical, chemical, and structural compositions and properties at the scale of the core sample. Shipboard measurements, such as those from the multisensor track (MST), provide high-resolution continuous records of these properties. Core measurements are especially useful at shallower depths where in situ logs cannot be recorded. At larger centimeter-to-meter scales, log data provide "ground truth" of in situ properties wherever the hole condition is reasonably good. Log data also bridge the resolution from the millimeter scale of core

[1]Fisher, A., Davis, E.E., and Escutia, C. (Eds.), 2000. *Proc. ODP, Sci. Results,* 168: College Station TX (Ocean Drilling Program).
[2]Lamont-Doherty Earth Observatory of Columbia University, P.O. Box 1000, Palisades NY 10964, USA. sunyf@ldeo.columbia.edu

sample to the meter scale of seismic data. Although the seismic resolution is comparatively low, it is an efficient means to trace the events identified from the well-log data beyond a drilled site and to construct spatially continuous maps of physical properties. Constrained by log and core data, the seismic data provide an important tool for regional investigation. Integration of core measurements and downhole log data has been increasingly exploited for estimation of permeability and thermal conductivity in hydrological and hydrothermal studies. Villinger et al. (1994) estimate in situ thermal conductivity of sediments from downhole logs. Fisher et al. (1994) measure sediment consolidation parameters to define rebound corrections for shipboard measurements of physical properties, including in situ void ratio (or porosity) and bulk density. Fisher et al. (1994) also develop relationships between effective stress and void ratio and between permeability and void ratio by means of consolidation and permeability tests.

Moore et al. (1995) obtain good agreement of log-derived fluid pressures with estimates from consolidation tests for Ocean Drilling Program (ODP) Leg 156. Many attempts have also been made to estimate in situ properties of sediments and natural rocks by integration of log and seismic data for diagnosis of crustal evolution, the history of deformation processes, and paleoceanographic applications (Bloomer and Mayer, 1997). Recently, seismic data have been used to evaluate the petrophysical properties of the formation (Rasmussen and Maver, 1996). Seismic inversion of porosity also promises to provide "continuous" two-dimensional (2-D) and 3-D models of permeability and thermal conductivity. Core-log-seismic integration is, therefore, arguably the best means to analyze and interpret these three independent data sets. This integration effort may also help to achieve a better understanding of the underlying mechanism of interactions between wave and pore-scale structures of the sediments/rocks, if theoretical models are successfully developed to link the measurements to intrinsic properties of the sediments, rocks, and pore fluids.

To accomplish this, we use an extended Biot theory of poroelasticity as a unifying theoretical model, because it can potentially deal with cases where solid suspensions in fluid or isolated fluid inclusions in solid are important (Sun, 1994; Sun and Goldberg, 1997b). Furthermore, even a very simplified version, which reduces formally to the Biot or Gassmann model, offers considerable insights on how to define and analytically determine key model parameters. There are thirteen model parameters that need to be defined in the complete formulation (Stoll, 1989); in the reduced model, there are seven or eight model parameters (Gassmann, 1951a, 1951b; White, 1983; Hamilton, 1971; Jarrard et al., 1989). So many parameters cause immense difficulty for practical applications, and often misunderstanding (Stoll, 1998), because the frame bulk and shear moduli remain largely unconstrained for individual cases (Bryan and Stoll, 1988).

We propose two analytical formulas for these frame moduli. The proposed model has eight parameters, which can, fortunately, be defined through core-log-seismic integration. These model parameters are grain density, grain bulk and shear moduli, fluid density and bulk modulus, porosity, and bulk and shear coupling coefficients. The latter two coupling coefficients are defined as flexibility factors. The first five parameters are solid and fluid properties that can be estimated from core measurements. Porosity can either be obtained from well log or derived from the shipboard gamma-ray attenuation porosity evaluator (GRAPE) density records. The flexibility factors can be determined using sonic acoustic and shear logs. If these data are not available, they may be estimated using core and seismic data by generalized nonlinear inversion (GNI), which optimizes these parameters to minimize the discrepancy between field seismic data and the synthetic seismograms generated using the theoretical model.

The methodology adopted in this report is summarized as follows. The (A) steps are applied to the logged site, and (B) steps are applied to sites without logging. The equations used are defined and referred to in the following sections.

1. Grain and fluid properties
   Calculate the average grain and fluid properties from discrete index property (IP) and digital sonic velocimeter (DSV) measurements; namely, grain density and grain *P*-wave velocity ($V_p$) and *S*-wave velocity ($V_s$), and fluid density and velocity. Where the DSV measurements are poor, the grain velocities $V_p$ and $V_s$ may be calculated theoretically from the mineral compositions of the core sample (e.g., Jarrard et al., 1989) or from other resources.
2. Bulk density
   A. Edit the density logs for hole-condition corrections.
   B. Edit the MST GRAPE density to ensure the data quality and eliminate unreasonable data points due to measurement errors. It is assumed that basic instrumental and environmental corrections have been routinely applied to the data (Boyce, 1976).
3. Porosity
   A. Edit the porosity logs for hole-condition corrections.
   B. Generate pseudoporosity log using the corrected GRAPE density log, the average grain density and fluid density, and the density-porosity relation (Eq. 19).
4. *P*-wave velocity
   A. Edit sonic $V_p$ logs for hole-condition corrections. Generate three crossplots: density and porosity logs, porosity and velocity logs, and density and velocity logs from separate runs, if available, to further reduce the effect of poor hole conditions. Also, generate an initial pseudovelocity log from corrected porosity logs using the proposed model with an initial value for the flexibility factor $\gamma$. Use the GNI scheme to optimize $\gamma$, minimizing the discrepancy between the true velocity log and the pseudovelocity log at the logged site.
   B. Use the final optimized flexibility factor $\gamma$ from the logged site as an initial $\gamma$ value, and use the data obtained in Steps 1–3 and Equations 17–23 and 27 to generate an initial pseudovelocity log.
5. Reflection-coefficient series
   A. Calculate reflection series using the corrected density and velocity logs and Equation 29.
   B. Calculate reflection series using the corrected density and pseudovelocity logs and Equation 29.
6. Synthetic seismogram
   Generate synthetic seismogram using Equation 30 and results from Step 5. The optimal center-frequency of the source wavelet can be estimated from spectral analysis of nearby seismic data.
7. GNI scheme
   A. Use the GNI scheme and Step 4A to make further corrections on $V_p$ logs for possible mismatch in traveltime.
   B. Use the GNI scheme to minimize the mismatch between the synthetic and field seismic data and optimize the flexibility factor $\gamma$ using Steps 4–7 iteratively. The optimal synthetic seismogram should have a better match with field data in traveltime and amplitude.
8. Further GNI optimization
   A. Use GNI scheme and repeat Steps 5–7 to optimize the source parameter and the center-frequency, and to obtain a better match of the synthetic with field seismic data in both waveform and amplitude.
   B. Repeat Steps 4–7 to optimize the source parameter and the center-frequency, and to obtain a better match of the synthetic with field seismic data in both waveform and amplitude.
9. Results
   A and B. Obtain the optimal flexibility factor $\gamma$, source center-frequency, synthetic seismogram, and the optimal high-resolution pseudovelocity log.

In the following sections, we present the theoretical model, the modeling results, and an analysis to illustrate the core-log-seismic integration method. Nine sites are studied along a transect extending more than 100 km eastward from the Juan de Fuca Ridge, drilled during ODP Leg 168 in 1996.

This transect penetrates sediments from a few meters to hundreds of meters thick overlying young oceanic crust of age 0.9–3.6 Ma in the eastern Pacific of 48°N (Fig. 1). To the best of our knowledge, it is the first time that good estimates of high-resolution porosity-depth and velocity-depth profiles have been used at sites without logging to construct synthetic seismograms in good agreement with field seismic data along such a long transect. We discuss the significance of the proposed velocity-porosity relationship and the important geological interpretation of the flexibility factor γ, which characterizes the softness or "uncompactedness" of the formation. We also point out some difficult problems that might be encountered in quantitative core-log-seismic integration aimed towards other sedimentary environments, such as the scale difference of core, log, and seismic data and the signal/noise ratio of seismic data.

## THEORETICAL BACKGROUND

Various investigations have developed empirical velocity-porosity relationships that are valid for only limited cases. The use of a time-average equation (Wyllie equation) to interpret sonic logs has been a standard practice in the oil industry for typical sedimentary rocks of intermediate (<40%) porosity (Wyllie et al., 1956; Schlumberger, 1989). Combining theoretical results from Gassmann theory of elastic waves in porous media with experimental ones from core, laboratory, and real seismic data, Hamilton gives many empirical relationships that have been used by many scientists in studies of marine sediments (Hamilton, 1971, 1976; Stoll, 1989; Jarrard et al., 1989; Hyndman et al., 1993; Sun et al., 1994; Guerin and Goldberg, 1996; etc.). Hamilton (1979) also reported $V_p/V_s$ and Poisson's ratios in marine sediments. Sun (1994) developed a dynamical theory of fractured porous media that generalizes Biot theory and Gassmann theory of porous media. In this report, we briefly review this dynamical theory and outline a simplified version of it. This theory is expected to be valid for marine sediments over a wide porosity range and in different sedimentary environments.

The basic theory of seismic-wave propagation is founded upon the equations of motion of classical continuum mechanics. The structural effects of individual defects, pores, or fractures and related dynamic instability have been studied only as boundary-value problems. Natural materials, however, are mixtures of different minerals with complicated porous and/or fracture structures. It is the pores, cracks, fractures, fissures, joints, faults, and other internal structures that are the vital elements for the storage and migration of subsurface fluids. Many theoretical studies of seismic properties of porous or fractured media, such as effective medium theories (e.g., Kuster and Toksöz, 1974; O'Connell and Budiansky, 1974; Bruner, 1976; Hudson, 1980) and field theories (e.g., Kosten and Zwikker, 1941; Frenkel, 1944; Biot, 1956; Dvorkin and Nur, 1993), have been applied in experimental studies and in field examples with limited success. For example, the Biot theory (Biot, 1956), of which Gassmann theory is a special case, can be used phenomenologically to predict porosity from seismic velocities more accurately than the time-average equation (Wyllie et al., 1956), but physically cannot be used for rocks at low differential pressures (Gregory, 1976; Murphy, 1984; Sun, 1994). This limits the ability to obtain high-resolution petrophysical and stratigraphic information from seismic or well-log data. Biot theory of wave propagation in porous rock has gained increasing use in seismic reservoir modeling. However, the effects of fractures and cracks in natural rocks have been largely ignored in its development. To extend Biot theory, Sun (1994) developed a topological characterization of structural media that provides a representation of the internal structure of a fractured porous medium at a finer scale and investigated the general mechanics and thermodynamics of fractured porous media. This theory was intended to provide a unified theoretical model for the full porosity range of materials from low-porosity igneous rocks to highly unconsolidated sediments.

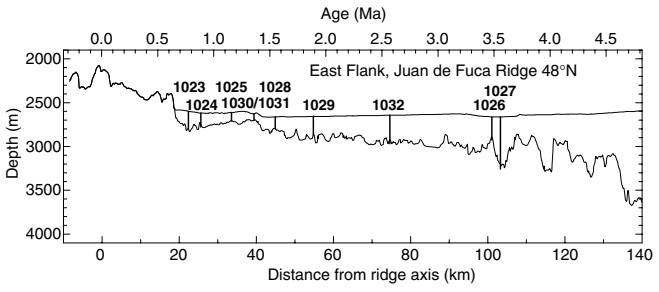


Figure 1. Locations of the sites of Leg 168 used for core-log-seismic integration.

In very simple terms, a porous medium with or without fractures consists of solid matrix and pore fluid. The physical properties of the composite (the porous medium) is determined by knowing the intrinsic properties of the solid grains and pore fluid, the parameters characterizing the structural effects, and the coupling coefficients between the solid grains and between the solid matrix and fluid. For low-porosity rock, like granites, the velocity change with pressure is mainly caused by change of the internal structures (cracks) under pressure. With increasing pressure, pre-existing cracks become collapsed and new cracks begin to form. Theoretical calculation of seismic velocities against measurements can give quantitative evaluation of the dynamic changes of aspect ratio with pressure and delineation of the undergoing deformation process (Sun and Goldberg 1997b). For high-porosity sediments or sedimentary rocks, velocity change with pressure is caused mainly by change of mechanical coupling between solid grains and the coupling between the pore fluid and grains (Geertsma and Smit, 1961; Domenico, 1977; Sun et al., 1994; Sun and Goldberg, 1997a). With an increase in depth, and therefore in pressure, sandy sediments become more rigid as the interlocking between grains and coefficient of sliding friction are increased. High-porosity silty clays and hemipelagic mud also gain rigidity and tightness through cohesion. More accurate quantification and estimation of sediment/rock properties can be obtained by a more detailed characterization of these coupling effects.

The interactions occurring in a porous medium with or without fractures are mathematically described as coupled effective macroscopic wave fields consisting of individual, microscopic fields that interact globally through volume averaging. From both the dynamic and constitutive equations, an extended Biot theory for a two-phase fractured porous medium (neglecting the intrinsic viscoelastic effects of each individual phase) is derived:

$$\begin{pmatrix}\rho^{11}\rho^{12}\\ \rho^{21}\rho^{22}\end{pmatrix}\frac{\partial^2}{\partial t^2}\begin{pmatrix}\mathbf{u^1}\\ \mathbf{u^2}\end{pmatrix} = \begin{pmatrix}P Q\\ Q R\end{pmatrix}\nabla\nabla\bullet\begin{pmatrix}\mathbf{u^1}\\ \mathbf{u^2}\end{pmatrix} - \begin{pmatrix}N T\\ T S\end{pmatrix}\nabla\times\nabla\times\begin{pmatrix}\mathbf{u^1}\\ \mathbf{u^2}\end{pmatrix} - \begin{pmatrix}b^{11}b^{12}\\ b^{21}b^{22}\end{pmatrix}\frac{\partial}{\partial t}\begin{pmatrix}\mathbf{u^1}\\ \mathbf{u^2}\end{pmatrix}, \quad (1)$$

where $\mathbf{u^1}$ and $\mathbf{u^2}$ are the solid and fluid displacements, respectively. The parameters in Equation 1 are dependent upon fundamental geometrical parameters $\chi^{ab}$ and $\phi^{ab}$ ($a, b = 1, 2$). These geometrical parameters are functions of the topological invariants of surfaces (or pore surfaces) and volume quantities. Physically, parameter $\chi^{ab}$ represents structural factors used to obtain an effective vector field such as particle velocity from averaging the vector fields of individual

phases. Parameter $\phi^{ab}$ represents structural factors used to obtain an effective tensor field such as stress from averaging the tensor fields of individual phases.

The detailed expressions of these quantities can be omitted for the practical applications in this report. *P, Q, R, N, S,* and *T* are also functions of intrinsic moduli of the solid and fluid.

For a two-phase isotropic fractured porous medium, the geometric parameter $\phi^{ab}$ can be specified as

$$\begin{pmatrix} \phi^{11} & \phi^{12} \\ \phi^{21} & \phi^{22} \end{pmatrix} = \begin{pmatrix} (1-\phi)(1-c_1) & \phi c_2 \\ (1-\phi)c_1 & \phi(1-c_2) \end{pmatrix}, \tag{2}$$

where $\phi$ is porosity (i.e., the volume fraction occupied by fluid), $c_1$ is the content of solid particles suspended in fluid, and $c_2$ is the content of fluid inclusions isolated in solid. However, the geometrical parameter $\chi^{ab}$ is symmetric (i.e., $\chi^{21} = \chi^{12}$, and $\chi^{12}$ is a real nonpositive number). And

$$\rho^{ab} = \rho^1 \chi^{1a} \chi^{1b} + \rho^2 \chi^{2a} \chi^{2b}, \ (a, b = 1, 2), \tag{3}$$

where $\rho^1$ and $\rho^2$ are defined as

$$\rho^a = \phi^{a1} \rho_0^1 + \phi^{a2} \rho_0^2, \ (a = 1, 2), \tag{4}$$

and $\rho_0^1$ and $\rho_0^2$ are the intrinsic density of the solid and fluid, respectively. If it is assumed that all the pores and fractures in a fractured porous medium are connected; that, more strongly, the space occupied by each phase is connected (i.e., $c_1 = c_2 = 0$), then the tensor $\phi^{ab}$ is uniquely determined by porosity $\phi$.

Using constraints on energy partition of relative motion and assuming that the flow in an individual pore is locally a Poiseuille flow, tensor $b^{ab}$ *(a, b* = 1, 2) becomes

$$\begin{pmatrix} b^{11} & b^{12} \\ b^{21} & b^{22} \end{pmatrix} = bF \begin{pmatrix} 1 & -1 \\ -1 & 1 \end{pmatrix}, \tag{5}$$

where *b* is a constant,

$$F \equiv \chi^2 \frac{\chi^2 \upsilon^2 \alpha - \chi^1 \upsilon^1}{\upsilon^1 - \upsilon^2 \alpha}, \tag{6}$$

$\upsilon^1$ and $\upsilon^2$ are the particle velocities of solid and fluid respectively, $\chi^1 = \chi^{11} + \chi^{21}$, $\chi^2 = \chi^{12} + \chi^{22}$, and $\alpha$ is the dynamic tortuosity defined as

$$\alpha = \frac{1}{|\cos\theta|}, \tag{7}$$

where $\theta$ is the angle between the velocity of the fluid and that of the solid. Therefore, $b^{ab}$ *(a, b* = 1, 2) are nonlinear functions of particle velocities of both solid and fluid phase.

The general wave equation, Equation 1, admits four kinds of elastic waves: the fast and slow *P*-waves and the fast and slow *S*-waves. This equation in its present form involves far more parameters than the Biot model, which represents the inherent properties of a fractured porous medium. As a forward problem, any given set of all these parameters specifies a concrete model. Nevertheless, it has to be simplified to be compared with experimental results and be practically useful. Because fluids do not possess intrinsic rigidity, it can be assumed that the intrinsic shear moduli of the fluids are negligibly small. By further assuming that the shear moduli acquired by fluids through coupling with the solids are also negligibly small, Equation 1 becomes

$$\begin{pmatrix} \rho^{11} & \rho^{12} \\ \rho^{21} & \rho^{22} \end{pmatrix} \frac{\partial^2}{\partial t^2} \begin{pmatrix} \mathbf{u}^1 \\ \mathbf{u}^2 \end{pmatrix} = \begin{pmatrix} P & Q \\ Q & R \end{pmatrix} \nabla\nabla \bullet \begin{pmatrix} \mathbf{u}^1 \\ \mathbf{u}^2 \end{pmatrix}, \tag{8}$$
$$- \begin{pmatrix} N & 0 \\ 0 & 0 \end{pmatrix} \nabla \times \nabla \times \begin{pmatrix} \mathbf{u}^1 \\ \mathbf{u}^2 \end{pmatrix} - bF \begin{pmatrix} 1 & -1 \\ -1 & 1 \end{pmatrix} \frac{\partial}{\partial t} \begin{pmatrix} \mathbf{u}^1 \\ \mathbf{u}^2 \end{pmatrix}$$

which is in the same form as the Biot equation of poroelasticity (Biot, 1956). The solution of this special wave equation admits three kinds of elastic body waves, namely, the fast and slow compressional waves and the shear wave. The notation used here in Equation 8 conforms to that used by Johnson and Plona (1982).

Although it is not different from the Biot equation in its form, Equation 8 has an advantage that all its phenomenological parameters can be defined explicitly in terms of the fundamental geometrical parameters of the internal structures and the physical parameters of the solid and fluid components. The shear modulus of the fractured porous medium is expressed as a function of the shear modulus of the solid as well as the geometry of internal structures. We assign $\psi^{ab} = \chi^{ca} \phi^{cb}$ and

$$\beta = \psi^{11} - \frac{\psi^{12} \psi^{21}}{\psi^{22}}, \tag{9}$$

so that

$$N = \beta \mu_0^1, \tag{10}$$

$$R = (\psi^{21} \alpha_p + \psi^{22}) K_0^{22}, \tag{11}$$

$$Q = (\psi^{11} \alpha_p + \psi^{12}) K_0^{22}, \tag{12}$$

and

$$P = \beta K_0^{11} + \frac{\psi^{12}}{\psi^{22}} Q + \frac{4}{3} N, \tag{13}$$

where $\mu_0^1$ is the intrinsic shear modulus of the solid, and $K_0^{11}$, $K_0^{22}$, and $\alpha_p$ are functions of the intrinsic bulk moduli of the solid ($K_0^1$) and fluid ($K_0^2$). *P, Q,* and *R* are also explicit functions of the effective geometrical parameter ß.

The velocities of the fast *P*-wave ($V_{p^+}$), slow *P*-wave ($V_{p^-}$), and *S*-wave ($V_s$) from Equation 8 can be expressed explicitly using the above parameters as

$$V_s^2 = \frac{\beta}{1 - \phi + (1 - \alpha^{-1}) \chi \phi} \frac{\mu_0^1}{\rho_0^1}, \tag{14}$$

and

$$V_{p\pm}^2 = V_{p^*}^2 \pm \sqrt{V_{p^*}^4 - \frac{\alpha^{-1}}{1 - \phi + (1 - \alpha^{-1}) \chi \phi} \left( \frac{P}{\rho_0^1} \frac{R/\phi}{\rho_0^2} - \frac{Q}{\rho_0^1} \frac{Q/\phi}{\rho_0^2} \right)}, \tag{15}$$

where

$$\begin{aligned} 2V_{p^*}^2 = & \frac{1}{1 - \phi + (1 - \alpha^{-1}) \chi \phi} \frac{P}{\rho_0^1} \\ & + \frac{(1-\phi)\alpha^{-1} + (1 - \alpha^{-1}) \chi \phi}{1 - \phi + (1 - \alpha^{-1}) \chi \phi} \frac{R/\phi}{\rho_0^2}, \\ & + 2 \frac{1 - \alpha^{-1}}{1 - \phi + (1 - \alpha^{-1}) \chi \phi} \frac{Q}{\rho_0^1} \end{aligned} \tag{16}$$

where $\rho_0^1$ and $\rho_0^2$ are the intrinsic mass densities of the solid and fluid respectively, fluid content $\chi = \rho_0^2 / \rho_0^1$, and $\phi$ is porosity. *P, Q,* and *R* are also explicit functions of the effective geometrical parameter $\alpha$ and ß. As expected, $\alpha_p$, ß, and tortuosity $\alpha$ depend upon aspect ratio and differential pressure, which characterize the effects of the solid/solid and solid/fluid couplings on seismic waves.

Equations 14 and 15 have been successfully used to investigate velocity-porosity and velocity-pressure relationships for igneous and sedimentary rocks with porosities ranging from 1% to more than 20% (Sun, 1994; Sun and Goldberg, 1997b). They can also be used to estimate variations of aspect ratio with pressure from velocity-depth or

velocity-pressure profiles (Sun and Goldberg, 1997a). Even though the existence of slow compressional wave in a water-saturated porous medium consisting of fused glass beads has been proven in laboratory experiments (Plona, 1980), there is not enough evidence that slow waves in natural marine sediments can be observed (Stoll, 1998). Therefore, we consider only propagation of the fast compressional and shear waves in sediments, and the two-phase medium can be further simplified as an effective medium. To simplify our notations to those commonly used in the literature, let $\rho_s$, $K_s$, and $\mu_s$ denote the density, bulk modulus, and shear modulus of the solid grains respectively; and let $\rho_f$ and $K_f$ denote the density and bulk modulus of the pore fluid, respectively. Then Equations 14 and 15 reduce to

$$V_p = \sqrt{\frac{K + \frac{4}{3}\mu}{\rho}} \tag{17}$$

and

$$V_s = \sqrt{\frac{\mu}{\rho}}, \tag{18}$$

where

$$\rho = (1-\phi)\rho_s + \phi\rho_f, \tag{19}$$

$$K = (1-\phi_k)K_s + \phi_k K_f, \tag{20}$$

$$\phi_k = F_k \phi, \tag{21}$$

$$F_k = \frac{1-(1-\phi)^{\gamma_k}}{[1-(1-\phi)^{\gamma_k}]\frac{K_f}{K_s} + \left(1-\frac{K_f}{K_s}\right)\phi}, \tag{22}$$

and

$$\mu = \mu_s (1-\phi)^{\gamma_k}. \tag{23}$$

The two parameters $\gamma_k$ and $\gamma_\mu$ are bulk and shear coupling coefficients respectively. We call these coupling coefficients the flexibility factors. They characterize the flexibility of the skeletal frame when subject to compressional and shear motion, respectively. The larger the values, the more flexible the frame for a given porosity, pressure, and temperature. Physically, this implies that the harder the formation (better coupling), the smaller the values of these flexibility factors. Note that the parameters $\phi_k$ and $F_k$ can be interpreted as effective porosity and effective coupling factor for the bulk modulus or for the compressional motion. Equations 20–22 can also be derived from Biot or Gassmann equation by letting simply the frame bulk modulus

$$K_b = K_s (1-\phi)^{\gamma_k}. \tag{24}$$

Equations 23 and 24 can be obtained using an analysis analogue to that given by Biot and Willis (1957), assuming that the two parameters $\gamma_k$ and $\gamma_\mu$ are not functions of porosity. In general, these two parameters are also functions of porosity and other geometrical factors, and Equations 23 and 24 will be in more complicated forms. These two simple equations reveal quantitatively how porosity and other geometrical factors affect the mechanical responses of a porous medium to external motion. Equation 23 states that even high-porosity unconsolidated sediments acquire rigidity that increases rapidly as porosity decreases or pressure increases. This agrees with many published works on the elastic properties of sediments (e.g., Hamilton, 1971; Stoll, 1989).

It should be noted that Equations 17–23 define the compressional and shear wave velocities in terms of intrinsic solid and fluid properties and geometrical factors, which are valid in principle for the entire porosity range from pure solid ($\phi = 0$) to pure fluid ($\phi = 1$). However, when used in practice, caution should be taken because these expressions have been obtained using many simplifications, even oversimplifications. For example, the effects of solid suspensions in fluid and isolated fluid inclusions in solid given in Equation 2 are neglected. This means that both the connectivity of the fluid phase and the connectivity of the solid phase are assumed to be perfect. In retrospect, however, Equations 23 and 24 can be generalized to be suitable for many practical situations,

$$\mu = (1-\phi)\mu_s f_\mu(\phi, G, P, T) \tag{25}$$

and

$$K_b = (1-\phi)K_s f_k(\phi, G, P, T), \tag{26}$$

where $f_k$ and $f_\mu$ denote pure geometrical effects that are functions of pressure $P$, temperature $T$, porosity $\phi$, and other geometrical factors $G$. Whereas the more complicated formulation for bulk modulus in Equations 20–22 are derived from the stress-strain relation of poroelasticity, the geometrical effects on wave velocities are essentially characterized by Equations 23–26 for frame moduli in the context of Biot field theory. Equations 23–26 show that the resistance of a skeletal frame to shear motion has the same expression as the resistance of the skeletal frame to compressional motion. This may suggest that the dependence of shear modulus $\mu$ on geometrical factors and that of frame bulk modulus $K_b$ could originate from the same causes due to the geometrical changes of internal pore structures under pressure. Such dependence is physically and mechanically different from that of gross bulk modulus K.

When measurements on shear wave velocity are not available, we assume, as a first-order approximation,

$$\gamma_\mu = \gamma_k \equiv \gamma, \tag{27}$$

or more generally,

$$f_\mu = f_k = f. \tag{28}$$

It means that the Poisson's ratio of the skeletal frame under a jacketed test is the same as the Poisson's ratio of the solid grain. Even though this agrees with common practice in practical applications, this assumption needs to be scrutinized by experiments and field data validation. We expect that it is applicable for sediments and high-porosity rocks. However, independent measurements of shear wave velocity are necessary to determine these flexibility factors for more detailed analysis.We will use Equations 17–23 as the theoretical working model for subsequent core-log-seismic integration. The intrinsic solid and fluid parameters (total of five) will be taken from core measurements. Porosity will be obtained either from well log or derived from shipboard high-resolution GRAPE density records with corrections for in situ conditions. Because there is no shear wave log and only core measurements available at the drilled sites of ODP Leg 168, the constraints on the shear flexibility factor $\gamma_\mu$ are inadequate. We will use the approximation formula in Equations 27 or 28 in the absence of these constraints.

## MODELING RESULTS AND DATA ANALYSIS

The sedimentary section drilled at nine sites during ODP Leg 168 provides an ideal opportunity to investigate the elastic properties of marine sediments. These nine sites span a 100-km transect on the east flank of the Juan de Fuca Ridge (48°N; Fig. 1). The depth of the sedimentary section varies from a few tens of meters to more than

500 m. The sediments encountered at all sites are composed mostly of interbedded sequences of hemipelagic mud (clayey silt to silty clay), sand turbidites, and silt turbidites (Davis et al., 1997). The deepest hole drilled during this leg is at Site 1027 where hemipelagic mudstone ~100 m thick was recovered below sandy and silty turbidites, before reaching basalt talus within thin interbeds of pelagic and hemipelagic mudstone at a depth of 569 m below seafloor (mbsf). The underlying basaltic basement ranges from 0.9 to 3.6 Ma eastward along the transect (Fig. 1).

## Core-Log-Seismic Integration at Logged Hole 1032A

Hole 1032A was the only hole logged during ODP Leg 168. It is located at 47°47′N, 128°07′W and was drilled to 338.4 mbsf and reached basement at 290.29 mbsf. Coring began at 184.53 mbsf, and the hole was logged to 283.9 mbsf. Bridging problems in the deeper part of the section thwarted all efforts to log deeper. Both the caliper log and heave record indicate a fairly good drilling environment and hole conditions through out the logged section (28- to 30-cm hole diameter), except in the deeper part of the hole. The density log (Fig. 2) was recorded using Schlumberger high-resolution hostile environment lithodensity sonde (HLDS) with 2.5-cm sampling interval.

The neutron porosity log was recorded using Schlumberger high-resolution accelerator porosity sonde (APS) with 5-cm sampling interval. The sonic velocity log ($V_p$) was recorded by the long-spacing array of the Schlumberger digital sonic tool (SDT) with sampling resolution of 15 cm. The overall quality of the log data is quite suitable for core-log-seismic integration, except in a few depth intervals where hole conditions were poor. Using the density and $V_p$ logs, the seismic reflection coefficient (RC) series can be calculated as

$$r_i = \frac{Z - Z_{i-1}}{Z + Z_{i-1}}, \tag{29}$$

where $Z_i = \rho_i v_i$ is the acoustic impedance, and $\rho_i$ and $v_i$ are the density and velocity at the discrete depth $i$, respectively. This $r_i$ series in depth can be converted to a series $r_n$ in two-way traveltime using the velocity profile. The latter is then convolved with a waveform to obtain a synthetic seismogram,

$$y_n = \sum_{m=0}^{n} r_m w_{n-m}, \tag{30}$$

where $w$ is the wavelet and $y$ is the synthetic seismogram. We use Ricker wavelet characterized by a single parameter, center-frequency, for the source waveform to generate synthetic seismograms in this report.

In Figure 2, the synthetic seismogram is compared with the shotpoint data from near Hole 1032A. The shotpoint seismic data were collected in 1995 by the University of Bremen, Germany. A 1.5-L (90 in$^3$) generator-injector (GI) gun source was used for the seismic source. The gun was supplied with compressed air at a pressure of 11.72 MPa and fired at 25-m shot spacing at nominally 10-s intervals. The data were acquired digitally with 20-bit floating point resolution at 6-kHz sampling frequency and then low-pass filtered and recorded at 2-ms sampling interval (Davis et al., 1997). Because these single-channel seismic data have a high signal/noise ratio, as seen on the 2-D section, no noise reduction filtering was applied, and the original amplitude information is preserved as much as possible. The synthetic seismogram is generated iteratively using a generalized nonlinear inversion algorithm (GNI; Press et al., 1992). The center-frequency of the Ricker wavelet is optimized to obtain a best fit between synthetic seismogram and the field data by assuming initially that the impedance model derived from the logs is fairly accurate. The initial center-frequency of the wavelet is estimated using spectral analysis of the field seismic data to be about 40 Hz. The seismic traveltime and amplitude of the synthetic are controlled by impedance contrast between subsurface layers. Because no cores or logs are available above 74.83 mbsf, no synthetic seismograms can be generated above this depth with the exception of the seawater/seafloor reflection. This is simulated by specifying $\rho = 1.7$ g/cm$^3$ and $v = 1665$ m/s for the sediment at depth 0 mbsf. Note that the seismograms have been converted to depth in all the following illustrations, unless specified otherwise.

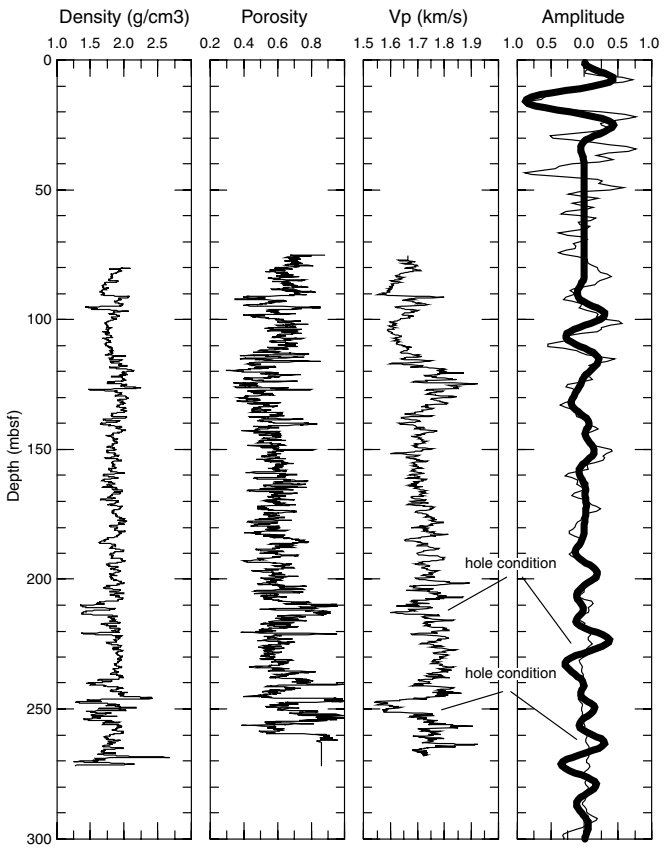


Figure 2. Comparison of field seismic data (thin line) with synthetic seismogram (thick line) generated using log data at Site 1032: HLDS density log, APS neutron porosity log, and SDT sonic velocity. The indicated mismatches are caused by unfavorable hole conditions.

The comparison of synthetic data with the field trace in Figure 2 is generally of high quality. In two intervals indicated on the figure, poor hole conditions precluded a good correlation. For the interval below 200 mbsf, we use both moving-window averaging and density-$V_p$ crossplot to make corrections on the sonic and density logs. Both the corrected density and velocity logs are shown in Figure 3. The corrected density and $V_p$ logs are converted to reflection coefficients using Equation 29, and a synthetic trace is then generated using Equation 30. The RC series is fed into the GNI scheme to check the mismatch between the field seismic trace and the synthetic. The corrected synthetic seismogram agrees with field seismic data much better in the deeper part of the hole than in Figure 2. To estimate the porosity in these intervals, the corrected density log and the known average grain and fluid densities, $\rho_s = 2.68$ g/cm$^3$ and $\rho_f = 1.04$ g/cm$^3$, are used to generate a corrected porosity log below 200 mbsf. In Figure 3, both the corrected density and porosity profiles agree very well with discrete laboratory IP measurements. The laboratory DSV measurements of *P*-wave velocity, however, are lower than downhole sonic $V_p$ log.

To ensure that the corrected density, porosity, and velocity logs are consistent, we extend this derivation of porosity from the density

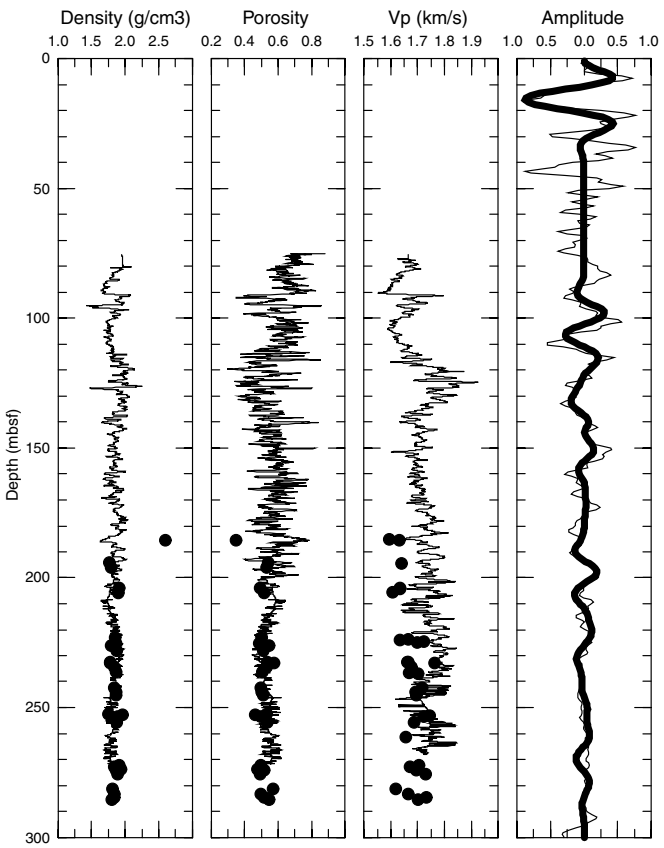


Figure 3. Comparison of field seismic data with synthetic seismogram generated using density and velocity logs at Site 1032, corrected only below 200 mbsf. Discrete sample points are laboratory IP and DSV measurements.

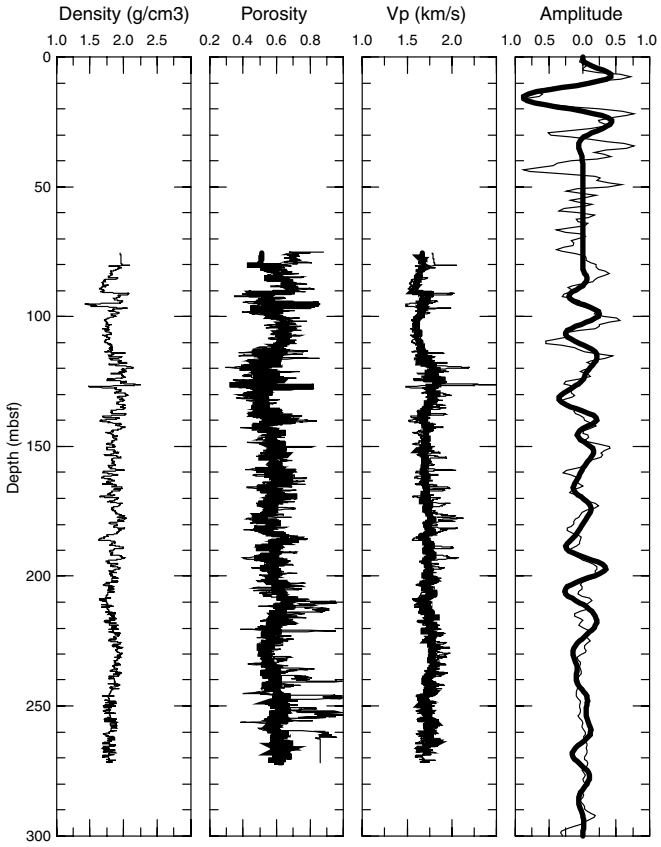


Figure 4. Comparison of field seismic data with synthetic seismogram generated using pseudoporosity and pseudovelocity logs, Site 1032. Pseudoporosity profile (thick line) overlaps with the downhole porosity log (thin line). Pseudovelocity also coincides with the downhole sonic velocity log.

over the entire logged interval from 80 to 272 mbsf. A pseudoporosity log is shown in Figure 4 and generally agrees well with the downhole porosity log (except in the intervals of borehole washout). We use the pseudoporosity log and the theoretical model to calculate a predicted *P*-wave velocity. This is achieved by using the GNI scheme to optimize the error between the $V_p$ log and the predicted *P*-wave velocity for an optimal flexibility factor γ. The estimate flexibility factor γ is 7.0 at this site. For a more accurate analysis, γ should vary with depth. As shown in Table 1, the γ value at this site is the lowest among the nine sites, which indicates that the sediment column at this site is the most compacted of those drilled during Leg 168. The model parameters needed for the theoretical calculation of the $V_p$ and synthetic seismogram are also summarized in Table 1. The predicted $V_p$ from this calculation approximates the downhole $V_p$ log well and is shown in Figure 4. It also agrees well with the seismically corrected $V_p$ log for the depth interval below 200 mbsf (see Fig. 3). Figure 4 also shows that the synthetic seismogram generated using the pseudovelocity log matches the field seismic trace. Figure 5 indicates that the shipboard-measured GRAPE density agrees well with the downhole density log below 180 mbsf. This suggests that GRAPE density measurements need fewer corrections than velocity measurements performed in the laboratory.

Core-log-seismic integration at Hole 1032A illustrates that (1) seismic measurements can be used to aid log correction, (2) the theoretical model of depth- (or pressure-) dependent velocity-porosity relationships is valid for the sedimentary environment at this site, and (3) the same methodology may be usefully applied where there is no downhole velocity log.

## High-Resolution Porosity-Depth and Velocity-Depth Profiles at Holes Without Logging

Figures 4 and 5 suggest that GRAPE density data could be used to derive high-resolution porosity-depth and velocity-depth profiles at the other eight sites where there are no logs. Caution must be advised in applying this model at all the sites and to all the seismic data in this area because local in situ parameters are required as input into this model. The seismic source waveform should also be optimized site by site. In the following, we use two holes, Holes 1023A and 1027B, to illustrate the generalization of the method. These two holes are at the opposite ends of the transect (Fig. 1) and are separated from each other by about 80 km.

Figure 6 shows GRAPE density records and pseudoporosity and pseudovelocity profiles compared with discrete IP and DSV measurements at Site 1023. Excellent agreement is obtained between synthetic seismogram and field seismic trace in both traveltime and waveform amplitude in the entire sediment column. The high-resolution density, pseudoporosity, and pseudovelocity profiles obtained also agree well with the IP and DSV measurements below the depth of 130 mbsf. Figure 6 indicates that the elastic rebound corrections made on these IP and DSV measurements were underestimated above this depth and require correction before use for other purposes.

Results from Site 1027 are shown in Figure 7. GRAPE density records and pseudoporosity and pseudovelocity profiles are compared with discrete IP and DSV measurements. Reasonable agreement is also achieved between the synthetic seismogram and field seismic

**Table 1. Physical and seismic properties for core-log-seismic integration at Leg 168 sites.**

| Site: | 1023 | 1024 | 1025 | 1030 | 1028 | 1029 | 1032 | 1026 | 1027 |
|---|---|---|---|---|---|---|---|---|---|
| $\rho_s$ (g/cm$^3$) | 2.65 | 2.65 | 2.65 | 2.68 (2.70) | 2.68 (2.70) | 2.68 (2.73) | 2.68 (2.75) | 2.66 | 2.68 (2.73) |
| $V_{ps}$ (km/s) | 6.5 | 6.5 | 6.5 | 6.5 | 6.5 | 6.5 | 6.5 | 6.5 | 6.5 |
| $V_{ss}$ (km/s) | 3.3 | 3.3 | 3.3 | 3.3 | 3.3 | 3.3 | 3.3 | 3.3 | 3.3 |
| $\rho_f$ (g/cm$^3$) | 1.04 | 1.04 | 1.04 | 1.04 | 1.04 | 1.04 | 1.04 | 1.04 | 1.04 |
| $V_{pf}$ (km/s) | 1.5 | 1.5 | 1.5 | 1.5 | 1.5 | 1.5 | 1.5 | 1.5 | 1.5 |
| $\gamma$ | 15 | 15 | 15 | 15 | 15 | 10 | 7.0 | 10 | 10 |
| $F_c$ (Hz) | 60 | 60 | 60 | 60 | 60 | 60 | 40 | 60 | 30 |

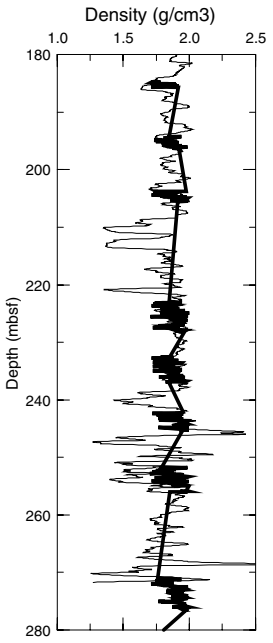


Figure 5. Comparison of downhole density log (thin line) with shipboard GRAPE density measurements (thick line). For depth intervals of no core recovery, interpolation is used for plotting purposes. These two density measurements agree with each other fairly well where hole conditions are favorable.

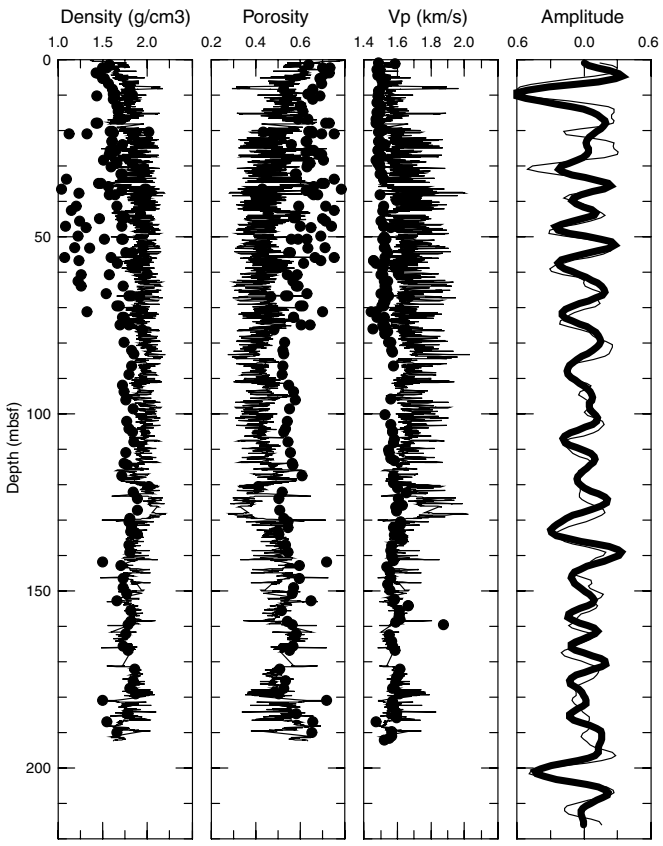


Figure 6. Comparison of field seismic data with synthetic seismogram generated using pseudoporosity and pseudovelocity profiles, Site 1023. GRAPE density is plotted against discrete IP density measurements. Pseudoporosity is vs. discrete IP porosity, and pseudovelocity against the discrete DSV data.

trace except at the depth interval from 100 to 240 mbsf where almost no core was recovered. The agreement between the synthetic and field seismic data for Hole 1023A (Fig. 6) and for Hole 1032A (Fig. 4) is much better than that at Site 1027. Although the traveltime and seismic amplitude agree well, the waveform does not match. The lack of core data in intervals where such discrepancies occur causes this disagreement. Instead of interpolating physical properties over these intervals, we infer the properties of sandy sediments to predict the traveltime and amplitude in the synthetic. Reasonable agreement with the field seismic data is possible; however, the high-resolution impedance changes are still lacking in these intervals. Where cores were recovered below 150 mbsf, density, pseudoporosity, and pseudovelocity profiles match with the core IP and DSV measurements. DSV measurements below 450 mbsf are generally higher than the pseudovelocity data. It is interesting to note that the velocity-porosity relationship in the model used is better than either Wood's model or Wyllie's model in representing these data (Fig. 8).

With successful integration of core-log-seismic data at these three holes, we gain confidence to apply our methods to the rest of the sites of ODP Leg 168. Figure 9 shows the GRAPE density records for the nine drilled sites. Site 1031 is omitted because it is very near to Site 1030. The pseudoporosity profiles and pseudovelocity profiles for all these sites are shown in Figures 10 and 11, respectively. Both these density-derived profiles have a sample interval of 5 cm. Figure 12 shows comparisons between synthetic seismograms and field seismic profiles at all sites, plotted in two-way traveltime. Overall, these profiles all agree reasonably well. Table 1 summarizes all the model parameters that are needed to obtain the porosity-depth and velocity-depth profiles at all sites. The average grain density measured on core samples from a given site is used for that site, without accounting for the mineral compositions, which needs to be improved for a more detailed analysis. Note that the grain densities averaged from core measurements for Holes 1030B, 1028A, 1029A, 1027B, and 1032A range from 2.70 to 2.75 g/cm$^3$, which are much higher than the average values expected for these sediments. A density of 2.68 g/cm$^3$ is used for these sites instead. The fluid densities are 1.040 g/cm$^3$, which is a good approximation for seawater at these depths (Pond and Pickard, 1978). The compressional and shear wave velocities of the solid grains are also assumed to be constant for all sites, which may not be necessarily accurate to estimate the grain elastic moduli. The estimated flexibility factor $\gamma$ for each site is also given. As the sedi-

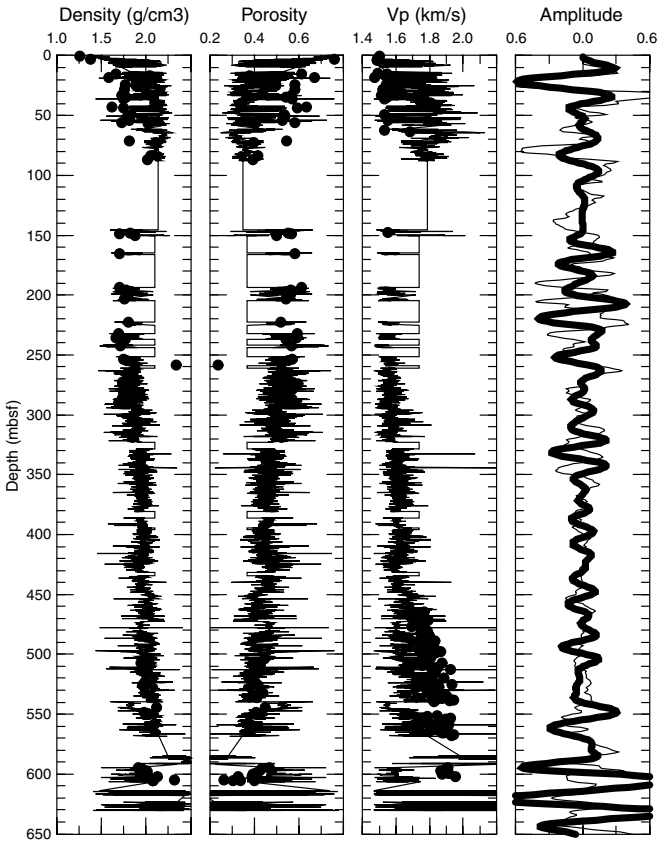


Figure 7. Comparison of field seismic data with synthetic seismogram generated using pseudoporosity and pseudovelocity profiles, Site 1027. GRAPE density is plotted against discrete IP density measurements. Pseudoporosity is vs. discrete IP porosity, and pseudovelocity against the discrete DSV data.

ment thickness increases eastward from Site 1023 to 1027, the estimated flexibility factor γ in this model decreases (see Table 1), which implies that the overall sediment column becomes tighter or more compacted from Site 1023 to 1027. The implications of these results are discussed below.

## DISCUSSIONS AND CONCLUSIONS

During Leg 168, only Hole 1032A was logged. We used density and sonic velocity logs to generate synthetic seismograms and compare them with field seismic data, using a generalized nonlinear inversion scheme. We are able to correct the logs for poor hole conditions and to correct both continuous and discrete shipboard core measurements for elastic rebound. We find that both continuous and discrete laboratory measurements of bulk density after rebound correction agree well with the downhole density log. We also use the density logs to obtain pseudoporosity profiles. The intrinsic properties of solid grains and pore fluid are determined from shipboard core measurements of sediments. Using a theoretical model and these pseudoporosity logs, we derive pseudovelocity logs using the GNI inversion scheme to optimize a flexibility factor γ, which characterizes the softness of the formation. We find that the elastic rebound corrections made on laboratory measurements (IP porosity and DSV velocity) at shallow depths were underestimated and caution should be taken if these discrete measurements are to be used. This core-log-seismic integration at Hole 1032A provides confidence that shipboard continuous density records (GRAPE density) could be used to obtain high-resolution porosity-depth profiles at the other sites where

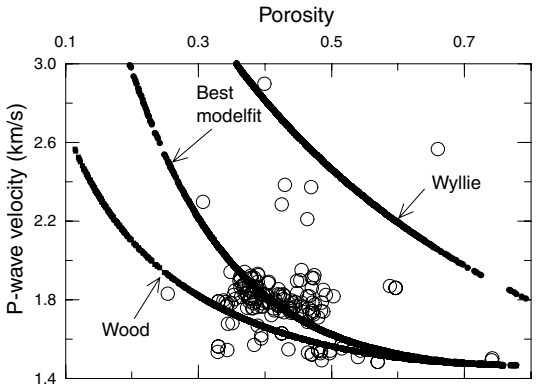


Figure 8. Velocity-porosity relationship at Site 1027. The discrete data are from DSV measurements.

no logs were available. The flexibility factor γ at each site is estimated through iterative comparison of synthetic and field seismograms using the generalized nonlinear inversion scheme. This enables us to obtain high-resolution velocity-depth profiles at all sites. Synthetic seismograms agree well with field seismic data not only in traveltime, but also in amplitude and waveform at all nine sites.

Through integrating core, log, and seismic measurements, we provide high-resolution velocity-depth and porosity-depth profiles for all the ODP Leg 168 sites. The high-resolution porosity-depth and velocity-depth profiles in the area can be interpolated to obtain a 2-D map of the depths to the sediment/basement contact. Further investigations of hydrological modeling and borehole observatory measurements could be aided using this information as input or constraints to construct accurate models of the sediment permeability and thermal conductivity structure in the area.

The flexibility factor γ we introduce in this simplified model provides a quantitative characterization of the softness or compaction state of the sediment column. For the Leg 168 transect, the γ values indicate that the sediment layers become more compacted as sediment thickness increases eastward and sediment ages become older. This qualitative observation between this flexibility factor and the sediment thickness and age may be expected; however, further investigation may unveil additional information from these profiles. The gamma value at Site 1032 is an exception to the general trend, because it is lower than values at Sites 1026 and 1027.

In this report, we did not use the seismic data to constrain the porosity-depth profiles from GRAPE density data. This could be done by a simultaneous optimization of both velocity and density profiles using more powerful, though more complicated, optimization schemes. Another important issue is the scale difference in bridging core, log, and seismic data. The core GRAPE density measurements and log data have a spatial resolution on the order of centimeters, whereas seismic resolution is on the order of 10 m, depending on the frequency. Although fine structures (<1 m thick) do not affect the traveltime of low-frequency seismic waves, a thin layer may strongly affect the amplitude and composite waveform of a seismic wavelet propagating through it. The mismatch in waveform and amplitude between the synthetic seismogram and field seismic data at Site 1027 is attributed to such thin layers, notably where high-resolution core information is missing. The noise in the field seismic data also affects the comparison of these results. Fortunately, the signal/noise ratio of the single-channel seismic data near the Leg 168 sites is quite acceptable for this comparison. It is expected, however, that an even better comparison could be obtained if seismic filtering had been applied to the data. This is not done, however, because filtering also distorts signal, especially at low and high frequencies that are vital to correlating the composite waveform and amplitude to core and log data.

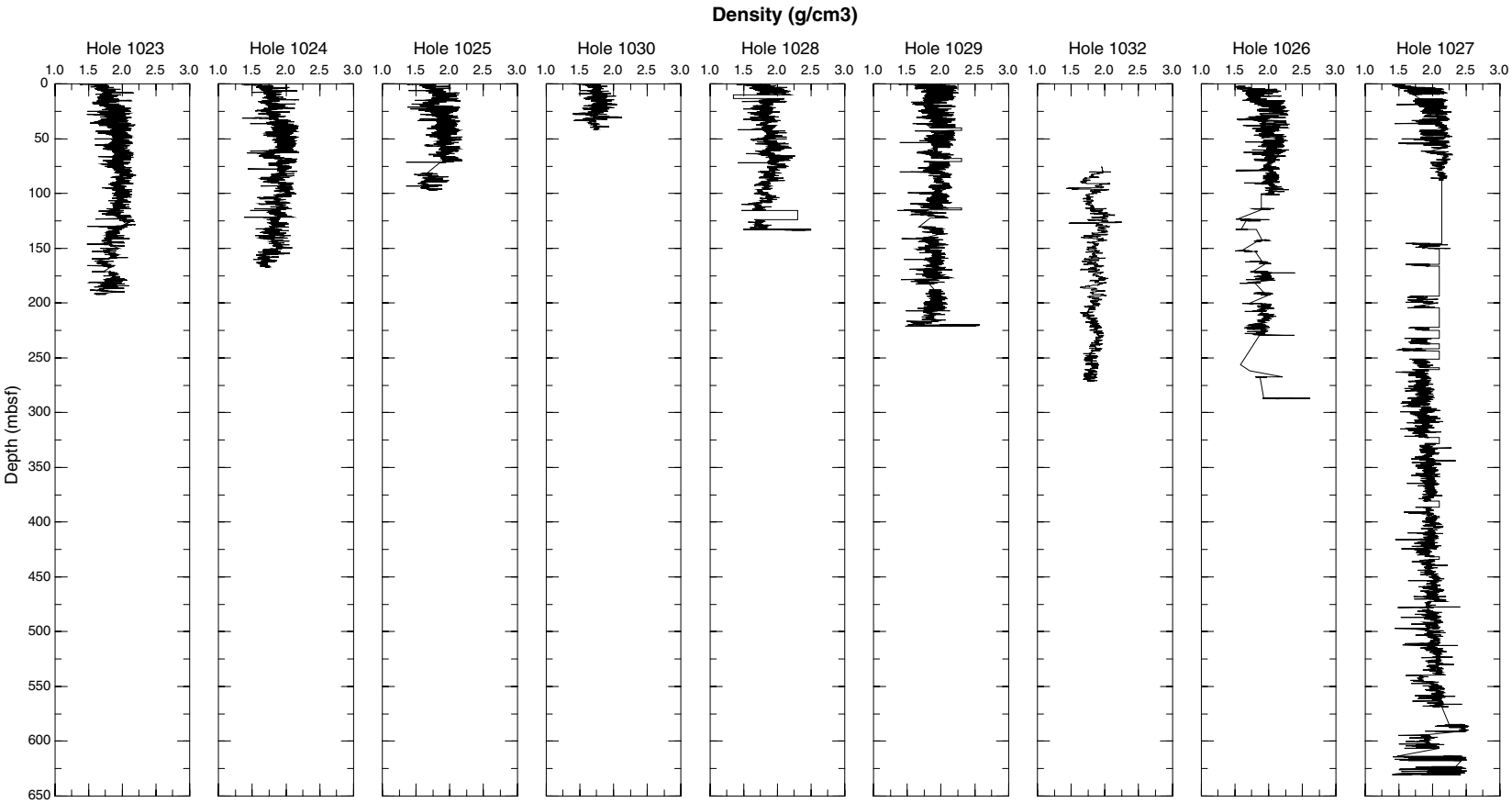


Figure 9. Density profiles at nine sites of Leg 168 used for core-log-seismic integration. Processed and corrected downhole density log is used for Hole 1032A. Corrected GRAPE density records are used for all other sites.

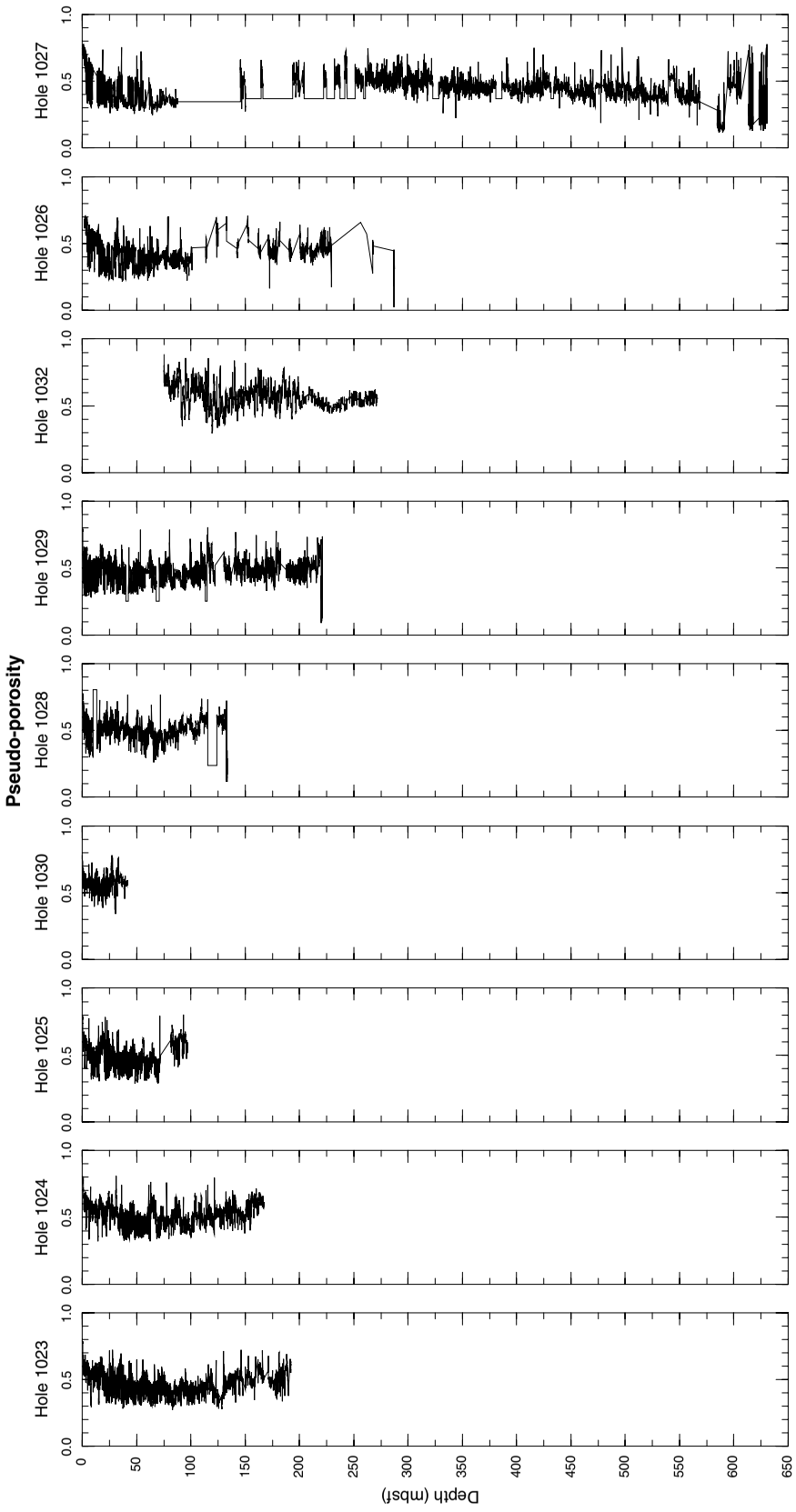


Figure 10. High-resolution (5-cm sampling interval) pseudoporosity profiles at nine sites of Leg 168 derived from density profiles in Figure 9. For the logged Hole 1032A, corrected downhole porosity log is shown. Resolution is 5 cm.

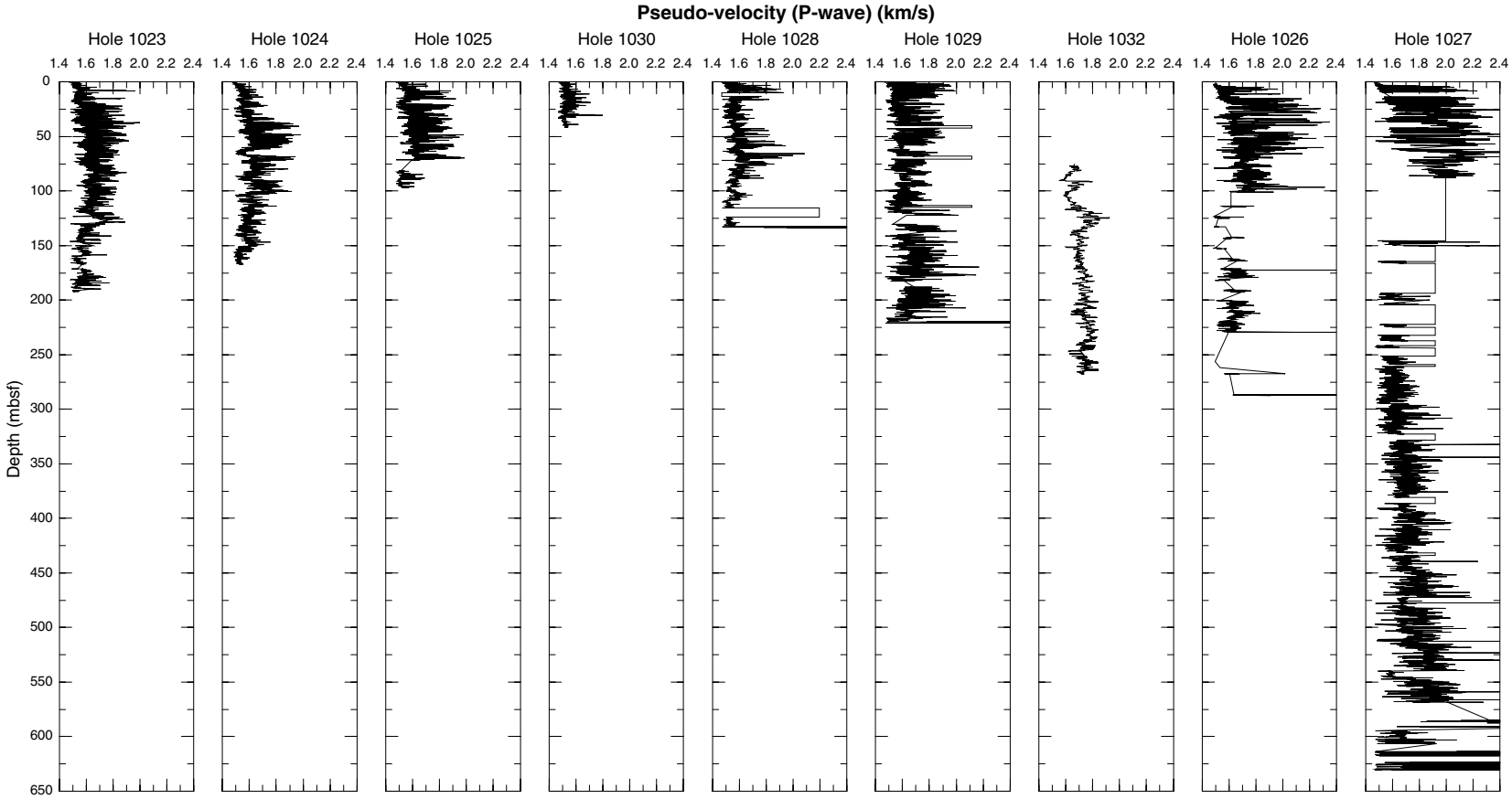


Figure 11. High-resolution pseudovelocity profiles at nine sites of Leg 168 derived from pseudoporosity profiles in Figure 10. For the logged Hole 1032A, corrected downhole $V_p$ log is shown. Resolution is 5 cm.

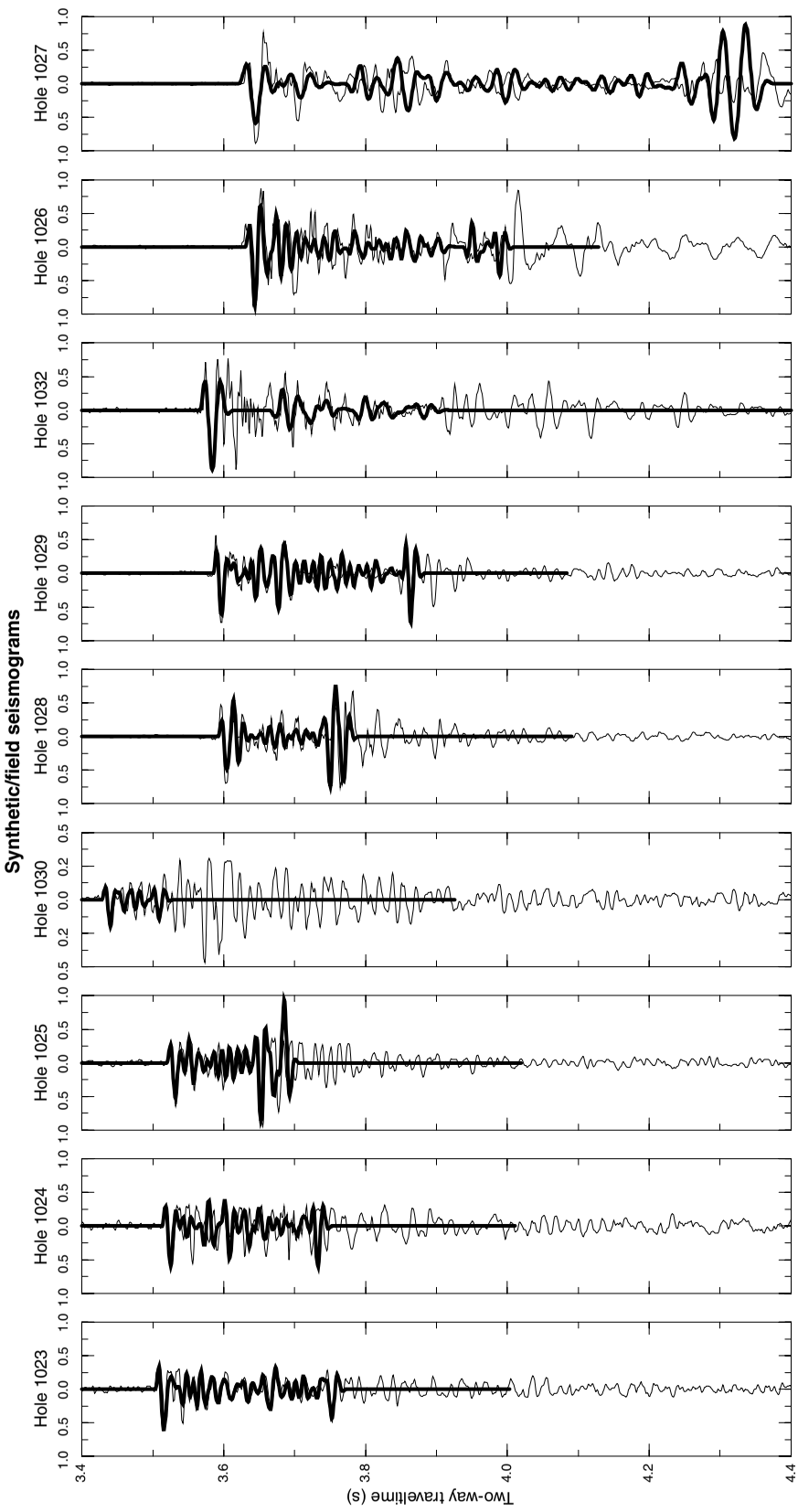


Figure 12. Comparison of field seismic traces (thin line) with synthetic seismograms (thick line) for all nine sites of Leg 168. The density profiles shown in Figure 9 and pseudovelocity profiles shown in Figure 11 are used to generate the synthetic data. For the logged Hole 1032A, downhole $V_p$ log is used.

We propose a velocity-porosity relationship for marine sediments along this 100-km-long transect of the Juan de Fuca Ridge. Compared with this relationship, Wyllie's time-average relation overestimates the velocity and Wood's equation underestimates the velocity at intermediate and low porosity. Wyllie's equation works well for intermediate porosity range and can be viewed as based on ray theory, although without a physical basis. Wood's equation is based on acoustic wave propagation and can be derived from the proposed model with some simplifications. Although the model parameters are site dependent, this relationship should be suitable for marine sediments in other similar environments. To a certain extent, this model can be viewed similarly to the Gassmann model, so that the results may be comparable with that obtained by Hamilton (1971) and Jarrard et al. (1989). However, their empirical fits for the frame bulk and shear moduli have only limited applicability. Here the frame moduli has a theoretical basis and is valid, in principle, for the full porosity range from 0% to 100%. In view of the assumptions used to derive these equations, the frame elastic moduli may not be adequate for all cases, but should have the same form as the general moduli discussed in previous sections. Further validation of this model and the methodology for core-log-seismic integration should be extended to sediments in other diverse environments and at other Deep Sea Drilling Project (DSDP) and ODP sites. In particular, the Leg 146 sediments in the Cascadia Basin, Leg 105 (Norwegian Sea), Leg 150 (New Jersey Margin), and other continental margin sediments may have adequate laboratory, log, and field seismic data to test the model without additional ship time.

## ACKNOWLEDGMENTS

The author would like to thank G. Eberli for making an effort to help measuring acoustic wave velocities under pressure on core samples, although limited success was achieved on only a few samples because of the technical difficulties of applying pressure on the highly unconsolidated sediments and mud. The core samples from ODP Leg 168 were kindly provided by the ODP core repository in College Station, Texas. The technical support from Leg 168 crew, staff, and colleagues is greatly acknowledged. The suggestions of reviewers H.J. Tobin and Nathan Bangs and Co-Chief A.T. Fisher are greatly appreciated. D. Goldberg and G. Myers provided thoughtful reviews. This research was supported by a JOI/USSAC grant. Lamont-Doherty Earth Observatory Contribution Number is 5944.

### REFERENCES

Biot, M.A., 1956. Theory of propagation of elastic waves in a fluid saturated porous solid, Parts I and II. *J. Acoust. Soc. Am.,* 28:168–191.

Biot, M.A., and Willis, D.G., 1957. The elastic coefficients of the theory of consolidation. *J. Appl. Mech.,* 24:594–601.

Bloomer, S.F. and Mayer, L.A., 1997. Core-log-seismic integration as a framework for determining the basin-wide significance of regional reflectors in the eastern equatorial Pacific. *Geophys. Res. Lett.,* 24:321–324.

Boyce, R.E., 1976. Definitions and laboratory techniques of compressional sound velocity parameters and wet-water content, wet-bulk density, and porosity parameters by gravimetric and gamma-ray attenuation techniques. *In* Schlanger, S.O., Jackson, E.D., et al., *Init. Repts. DSDP,* 33: Washington (U.S. Govt. Printing Office), 931–958.

Bruner, W.M., 1976. Comment on "Seismic velocities in dry and saturated cracked solids" by Richard J. O'Connell and Bernard Budiansky. *J. Geophys. Res.,* 81:2573–2576.

Bryan, G.M., and Stoll, R.D., 1988. The dynamic shear modulus of marine sediments. *J. Acoust. Soc. Am.,* 83:2159–2164.

Davis, E.E., Chapman, D.S., Villinger, H., Robinson, S., Grigel, J., Rosenberger, A., and Pribnow, D., 1997. Seafloor heat flow on the eastern flank of the Juan de Fuca Ridge: data from "FlankFlux" studies through 1995. *In* Davis, E.E., Fisher, A.T., Firth, J.V., et al., *Proc. ODP, Init. Repts.,* 168: College Station, TX (Ocean Drilling Program), 23–33.

Davis, E.E., and Villinger, H., 1992. Tectonic and thermal structure of the Middle Valley sedimented rift, northern Juan de Fuca Ridge. *In* Davis, E.E., Mottl, M.J., Fisher, A.T., et al., *Proc. ODP, Init. Repts.,* 139: College Station, TX (Ocean Drilling Program), 9–41.

Domenico, S.N., 1977. Elastic properties of unconsolidated porous sand reservoirs. *Geophysics,* 42:1339–1368.

Dvorkin, J., and Nur, A., 1993. Dynamic poroelasticity: a unified model with the squirt mechanism and the Biot mechanisms. *Geophysics,* 58:524–533.

Fisher, A.T., Fischer, K., Lavoie, D., Langseth, M., and Xu, J., 1994. Geotechnical and hydrogeological properties of sediments from Middle Valley, northern Juan de Fuca Ridge. *In* Mottl, M.J., Davis, E.E., Fisher, A.T., and Slack, J.F. (Eds.), *Proc. ODP, Sci. Results,* 139: College Station, TX (Ocean Drilling Program), 627–647.

Frenkel, J., 1944. On the theory of seismic and seismoelectric phenomena in a moist soil. *J. Physics (USSR),* 8:230–241.

Gassmann, F., 1951a. Elastic waves through a packing of spheres. *Geophysics,* 15:673–685.

————, 1951b. Über die Elastizität Poröser Medien. *Vierteljahrsschr. Naturforsch. Ges. Zuerich,* 96:1–23.

Geertsma, J., and Smit, D.C., 1961. Some aspects of elastic wave propagation in fluid-saturated porous solids. *Geophysics,* 26:169–181.

Gregory, A.R., 1976. Fluid saturation effects on dynamic elastic properties of sedimentary rocks. *Geophysics,* 41:895–921.

Guerin, G., and Goldberg, D., 1996. Acoustic and elastic properties of calcareous sediments across a siliceous diagenetic front on the eastern U.S. continental slope. *Geophys. Res. Lett.,* 23:2697–2700.

Hamilton, E.L., 1971. Elastic properties of marine sediments. *J. Geophys. Res.,* 76:579–604.

————, 1976. Variations of density and porosity with depth in deep-sea sediments. *J. Sediment. Petrol.,* 46:280–300.

————, 1979. $V_p/V_s$ and Poisson's ratios in marine sediments and rocks. *J. Acoust. Soc. Am.,* 66:1093–1101.

Hudson, J.A., 1980. Overall properties of a cracked solid. *Math. Proc. Cambridge Philos. Soc.,* 88:371–384.

Hyndman, R.D., Moore, G.F., and Moran, K., 1993. Velocity, porosity, and pore-fluid loss from the Nankai subduction zone accretionary prism. *In* Hill, I.A., Taira, A., Firth, J.V., et al., *Proc. ODP, Sci. Results,* 131: College Station, TX (Ocean Drilling Program), 211–220.

Jarrard, R.D., Dadey, K.A., and Busch, W.H., 1989. Velocity and density of sediments of Eirik Ridge, Labrador Sea: control by porosity and mineralogy. *In* Srivastava, S.P., Arthur, M.A., Clement, B., et al., *Proc. ODP, Sci. Results,* 105: College Station, TX (Ocean Drilling Program), 811–835.

Johnson, D.L., and Plona, T.J., 1982. Acoustic slow waves and the consolidation transition. *J. Acoust. Soc. Am.,* 72:556–565.

Kosten, C.W., and Zwikker, C., 1941. Extended theory of the absorption of sound by compressible wall-coverings. *Physica,* 8:968–978.

Kuster, G.T., and Toksöz, M.N., 1974. Velocity and attenuation of seismic waves in two-phase media, Part I: theoretical formulations. *Geophysics,* 39:587–606.

Moore, J.C., Shipley, T.H., Goldberg, D., Ogawa, Y., Filice, F., Fisher, A., Jurado, M.-J., Moore G.F., Rabaute, A., Yin, H., Zwart, G., and Brueckmann, W., Henry, P., Ashi, J., Blum, P., Meyer, A., Housen, B., Kastner, M., Labaume, P., Laier, T., Leitch, E.C., Maltman, A.J., Peacock, S., Steiger, T.H., Tobin, H.J., Underwood, M.B., Xu, Y., Zheng, Y., 1995. Abnormal fluid pressures and fault zone dilation in the Barbados accretionary prism: evidence from logging while drilling. *Geology,* 23:605–608.

Murphy, W.F., 1984. Acoustic measures of partial gas saturation in tight sandstones. *J. Geophys. Res.,* 89:11549–11559.

O'Connell, R.J., and Budiansky, B., 1974. Seismic velocities in dry and saturated cracked solids. *J. Geophys. Res.,* 9:5412–5426.

Plona, T.J., 1980. Observation of a second bulk compressional wave in a porous medium at ultrasonic frequencies. *Appl. Phys. Lett.,* 36:259–261.

Pond, S., and Pickard, G.L., 1978. *Introductory Dynamic Oceanography*: Oxford (Pergamon).

Press, W.H., Teukolsky, S.A., Vetterling, W.T., and Flannery, B.P., 1992. *Numerical Recipes in Fortran: the Art of Scientific Computing* (2nd ed.): New York (Cambridge Press), 180–184.

Rasmussen, K.B., and Maver, K.G., 1996. Direct inversion for porosity of post stack seismic data [paper SPE35509 presented at the European 3-D Reservoir Modelling Conference, Stavanger, Norway, April 1996].

Schlumberger, 1989. *Log Interpretation Principles/Applications:* Houston, TX (Schlumberger Educ. Services).

Stoll, R.D., 1989. *Sediment Acoustics:* New York (Springer-Verlag), Lecture Notes in Earth Sciences, 26.

————, 1998. Comments on "Biot model of sound propagation in water-saturated sand" [*J. Acoust. Soc. Am.,* 97:199–214 (1995)]. *J. Acoust. Soc. Am.,* 103:2723–2725.

Sun, Y.F., 1994. On the foundations of the dynamical theory of fractured porous media and the gravity variations caused by dilatancies [Ph.D. dissert.]. Columbia Univ., New York.

Sun, Y.F., and Goldberg, D., 1997a. Effects of aspect ratio changes on wave velocities in fractured rocks. *SEG Expanded Abstr.,* 67:925–928.

————, 1997b. Estimation of aspect-ratio changes with pressure from seismic velocities. *In* Lovell, M.A., and Harvey, P.K., (Eds.), *Development in Petrophysics.* Geol. Soc. Spec. Publ. London, 122:131–139.

Sun, Y.F., Kuo, J.T., and Teng, Y.C., 1994. Effects of porosity on seismic attenuation. *J. Comput. Acoust.,* 2:53–69.

Villinger, H.W., Langseth, M.G., Gröschel-Becker, H.M., and Fisher, A.T., 1994. Estimating in-situ thermal conductivity from log data. *In* Mottl, M.J., Davis, E.E., Fisher, A.T., and Slack, J.F. (Eds.), *Proc. ODP, Sci. Results,* 139: College Station, TX (Ocean Drilling Program), 545–552.

White, J.E., 1983. *Underground Sound: Application of Seismic Waves:* Amsterdam (Elsevier).

Wyllie, M.R.J., Gregory, A.R., and Gardner, L.W., 1956. Elastic wave velocities in heterogeneous and porous media. *Geophysics,* 21:41–70.

**Date of initial receipt: 9 December 1998**
**Date of acceptance: 9 December 1999**
**Ms 168SR-009**